Climate Dynamics (2026) 64:133
https://doi.org/10.1007/s00382-026-08116-0

ORIGINAL ARTICLE

Synergistic effect of El Niño and negative phase of arctic oscillation on winter precipitation over southern China

Xinxin Tang[1] · Jianping Li[1,2] · Yinan Yang[1] · Yang Zhao[1] · Yina Diao[1] · Hongyuan Zhao[1] · Yuan Liu[1]

Received: 12 September 2025 / Accepted: 13 February 2026

Abstract
We demonstrate that the negative phase of the arctic oscillation (AO^-) and El Niño exert a significant synergistic effect on the enhancement of winter precipitation over southern China (SCWP). The enhancement of SCWP under the co-occurrence of AO^- and El Niño arises from both the linear superposition of individual effects and nonlinear interaction between the AO^- and El Niño. Physical mechanisms reveal that El Niño favors the negative phase of North Atlantic Oscillation-like circulation, enhancing North Atlantic Rossby wave sources during the concurrent AO^-. Under the combined influence of AO^- and El Niño, Rossby waves initiated from central equatorial Pacific and subtropical North Atlantic synergistically intensified from North Atlantic to Eurasia in three pathways, facilitating the strengthening of a low-pressure anomaly over southern China and amplifies the tropical northwestern Pacific (TNWP) high. The intensified TNWP high is accompanied by stronger descending motion and anticyclonic circulation over the region, which increases southwesterly moisture transport toward southern China, and enhances ascending motion over southern China, leads to increased SCWP. By examining the synergistic effects of AO^- and El Niño on SCWP, this study advances our understanding of SCWP variability and its underlying mechanisms.

Keywords Southern China winter precipitation · Synergistic effect · El Niño · Arctic oscillation

1 Introduction

The variability of southern China winter precipitation (SCWP) is significant and has a major impact on agricultural production, water resource management, and ecosystem balance. Understanding the driving mechanisms behind its changes is crucial for improving forecast accuracy and formulating response strategies. The winter precipitation in southern China is influenced not only by atmospheric variability in the mid and high latitudes (He et al. 2017; Song et al. 2011), but also by the most dominant interannual variability in tropical sea surface temperatures, El Niño-Southern Oscillation (ENSO) (Wen et al. 2009; Li et al. 2013; Gao et al. 2020).

Both ENSO and the arctic oscillation (AO) play essential roles in modulating the wintertime climate over East Asia (Cheung et al. 2012; Huang et al. 2017aKim et al. 2021). El Niño is the dominant mode of interannual variability in tropical Pacific sea surface temperature (SST). Both observational analyses and numerical modeling studies have demonstrated that ENSO can induce significant climate anomalies across global scales, including China, resulting in droughts, floods, and temperature extremes, ultimately impacting industrial and agricultural productivity as well as societal functioning (Bjerknes 1969; Horel and Wallace 1981; Trenberth et al. 1998; Wang et al. 1999; Zhang et al. 1999). In the El Niño episode, the positive precipitation anomaly over the central-eastern equatorial Pacific promotes the development of an anticyclone over northwestern Pacific. This anticyclone anomaly drives northward moisture transport along its western boundary, directly contributing to SCWP enhancement (Zhang and Sumi 2002; Zhou et

✉ Jianping Li
ljp@ouc.edu.cn

[1] Frontiers Science Center for Deep Ocean Multi-Spheres and Earth System (FDOMES), State Key Laboratory of Physical Oceanography, Academy of Future Ocean/College of Oceanic and Atmospheric Sciences, Center for Ocean Carbon Neutrality, Ocean University of China, Qingdao 266100, China

[2] Laboratory for Ocean Dynamics and Climate, Qingdao Marine Science and Technology Center, Qingdao 266237, China

Published online: 05 March 2026

al. 2010; Zhang et al. 2017). Furthermore, during El Niño events, the East Asian winter monsoon weakens and the Pacific Walker circulation weakens. Meanwhile, El Niño causes the East Asian jet stream to shift southward and intensify, triggering anomalous upward motion that increases the frequency of extreme SCWP (Gao et al. 2020). El Niño can also synergistically influence SCWP in conjunction with extratropical circulation modes, such as the North Pacific Oscillation (Sun and Li 2022) and the AO (Zuo 2011; Chen et al. 2013).

The AO, as an extratropical hemispheric-scale mode, directly modulates mid-latitude circulation patterns (Thompson and Wallace 1998, 2001). The AO has significant impacts on East Asian weather and climate through the atmospheric changes including the Siberian high, upper-level trough, and westerly jet stream (Park et al. 2011; Lou et al. 2016; He et al. 2017). AO is closed related to North Atlantic Oscillation (NAO), and NAO is recognized to be the regional manifestation of AO in the North Atlantic Ocean (Kerr 1999). In winter, NAO can trigger the eastward propagation of Rossby waves along the Asian jet stream, establishing downstream teleconnections that significantly influence East Asian climate variability (Watanabe 2004; Xie et al. 2019; Li et al. 2022). During negative phases of the NAO, a pronounced precipitation deficit occurs across southwestern China through the Rossby wave energy propagation associated with NAO (Xu et al. 2012). Additionally, the AO can influence extreme precipitation in central and southern China by affecting the intensity and location of the mid-latitude westerly jet (Mao et al. 2011), the impact of which is even more significant than that of sea surface temperatures (SST) in the equatorial central and eastern Pacific and anomalies in the western Pacific subtropical high (Wen et al. 2009). Furthermore, the winter AO can influence East Asian extreme climate and winter monsoons by affecting Eurasian snow cover (Wang et al. 2022), Ural–Siberia blocking and the Siberian high pressure (Gong et al. 2001; Cheung et al. 2012).

Both ENSO and AO play an important role in East Asia climate, through their influence on Ural-Siberian blocking and East Asian winter monsoon (Cheung et al. 2012). It is found that when the negative phase of the AO (AO^-) and El Niño occur simultaneously, the SCWP increases significantly (Zuo 2011; Chen et al. 2013). However, whether the two factors exert a synergistic effect on SCWP remains to be determined, and the physical mechanism underlying the synergistic influence of $ENSO^+$ and the AO^- on SCWP is still unclear. Synergistic effects are an effective tool for explaining the variability of weather and climate in complex climate systems (Wang et al. 2022, 2023, 2024; Sun et al. 2022; Tang et al. 2023; Tang and Li 2024). A synergistic effect arising from two or more factors interacting or working together to produce an effect that is significantly greater than each of their individual effects (Li et al. 2019b). Due to the inherent nonlinear interactions between tropical and mid-to-high latitude atmospheric circulation modes (Wu and Lin 2012; Wu and Zhang 2015; Li et al. 2016), the synergistic influence of AO^- and El Niño on SCWP exhibits more complex characteristics. The synergistic effect can be understood in terms of both linear superposition and nonlinear response components. When the combined influence of these two factors surpasses the linear superposition of their individual effects, this nonlinear amplification implies the existence of complex nonlinear interactions within the climate system may be at play (Tang and Li 2024). Therefore, this study will analyze the synergistic effect of AO^- and El Niño on SCWP, and will investigate the physical processes underlying this synergistic effect. This research aims to deepen our understanding of the variability and underlying mechanisms of SCWP.

2 Data and methods

2.1 Datasets

The monthly precipitation data used in this study were obtained from the global monthly mean precipitation dataset of the ERA5 (the fifth-generation atmospheric reanalysis dataset by the European Centre for Medium-Range Weather Forecasts, ECMWF; https://cds.climate.copernicus.eu/datasets) (Hersbach et al. 2023). The winter season is defined to be 4 months in length, covering November through to the following February (NDJF). The data has a horizontal resolution of 1.0° × 1.0° and covers the period from January 1979 to December 2021. Atmospheric variables were obtained from the National Centers for Environmental Prediction–National Center for Atmospheric Research reanalysis dataset with a horizontal resolution of 2.5° × 2.5°.The AO index is defined as the difference in normalized zonally averaged Sea Level Pressure between 35 and 65°N (Li and Wang 2003). As the AO shows considerable intraseasonal and monthly variability, it is necessary to evaluate the AO time series on a monthly basis within a given winter season. The AO^- is defined when the standardized AO index falls below –0.7 (Table 1). The Oceanic Niño Index (ONI; https://origin.cpc.ncep.noaa.gov/products/analysis_monitoring/ensostuff/ONI_v5.php) provided by the Climate Prediction Center (CPC) is used to classify ENSO warm ($ENSO^+$) events. This index is derived from the three-month running mean of SST in the Niño 3.4 region (5°N–5°S, 120°W–170°W), based on the ERSST.v5 SST dataset (Huang et al. 2017b). Years with ONI values greater than 0.7 are classified as strong El Niño ($ENSO^+$) years (Table 2). According to this

Table 1 Classification of monthly/annual AO negative phases

AO^-			
Nov	Dec	Jan	Feb
1985	1980	1979	1979
1995	1989	1981	1982
2000	1995	1984	1984
2006	1996	1995	1985
2010	2000	1996	1993
2012	2001	1997	2004
2018	2005	2003	2009
2019	2009	2009	
	2010	2010	
	2012		

Table 2 Classification of $ENSO^+$ winters (NDJF) during 1979–2021, with years corresponding to November–December (ND) months

Events	Year
$ENSO^+$	1982, 1986, 1987, 1991, 1994, 1997, 2002, 2004, 2006, 2009, 2015, 2018

criterion, there are 12 strong El Niño years (Table 2). The Nino 3.4 index from the National Oceanic and Atmospheric Administration (NOAA) Physical Sciences Laboratory (https://psl.noaa.gov/data/timeseries/month) was used to represent ENSO variability.

2.2 Methods

2.2.1 Definition of synergistic effect

The concept of synergistic effects from Li et al. (2019b) is used in this study. A synergistic effect is an effect arising from two or more factors interacting or working together to produce an effect significantly greater than each of their individual effects. Let's consider two forcing events, denoted as X and Y. Here, the symbol $X \oplus Y$ represents the co-occurrence of both events X and Y, while $X \backslash Y$ refers to the situation where event X happens in isolation, without the occurrence of event Y. Similarly, $Y \backslash X$ represents the isolated occurrence of event Y without event X. Therefore, in this study, El Nino occur without AO^- is written to be $ENSO^+ \backslash AO^-$, $AO^- \backslash ENSO^+$ refers to individual events of AO^-, and $AO^- \oplus ENSO^+$ represents the joint events of AO^- and $ENSO^+$. We use $\delta_{Z,X}$ to represent the response of Z during the $X \backslash Y$ event, $\delta_{Z,Y}$ for the response during the $Y \backslash X$ event, and $\delta_{Z,X \oplus Y}$ for the response during the $X \oplus Y$ event. If the amplitude $|\overline{\delta_{Z,X \oplus Y}}|$ is significantly greater than the maximum of the amplitudes $|\overline{\delta_{Z,X}}|$ and $|\overline{\delta_{Z,Y}}|$, X and Y have a synergistic effect on Z. When $\delta_{Z,X \oplus Y}$, $\delta_{Z,X}$ and $\delta_{Z,Y}$ are of the same sign, their synergistic effect from X and Y is explicit synergism; otherwise, there might be an implicit synergistic effect (Li et al. 2019a, b). To better isolate the individual influence of $X \backslash Y$ (or $Y \backslash X$), before compositing the $X \backslash Y$ (or $Y \backslash X$) events, we remove the linear regression of Y (or X) on the monthly anomalies (Tang et al. 2023). This framework of synergistic effect has been widely applied across multiple research domains, including: winter precipitation (Sun and Li 2022; Tang et al. 2023, Tang and Li 2024), extreme heat/code events (Wang et al. 2022, 2023, 2024), and sub-seasonal forecasting enhancement (Qi et al. 2025).

To further understand the synergistic effect of two forcing factors, X and Y, on Z, the linear component of the response to the joint event $X \oplus Y$ is expressed as:

$$L_{Z,X \oplus Y} = \delta_{Z,X} + \delta_{Z,Y}, \tag{1}$$

The nonlinear response term is expressed as:

$$N_{Z,X \oplus Y} = \delta_{Z,X \oplus Y} - L_{Z,X \oplus Y}. \tag{2}$$

To measure the relationship between forcing and response anomalies to climatology for individual and joint events, as defined in Tang and Li (2024), local covariance between X and Z under joint events $X \oplus Y$ is defined as follows:

$$s_{X \oplus Y,zx} = \frac{1}{n_{xy}} \sum_{i=1}^{n_{xy}} z_{X \oplus Y,i}{}' x_{X \oplus Y,i}{}' \tag{3}$$

in which ' ' indicate anomalies to climatology. Similarly, we can get local covariance between Y and Z under joint or individual events of X and Y, as well as local covariance between X and Z under $X \oplus Y$ or $X \backslash Y$ events.

2.2.2 Significance test

Bootstrap methods are employed to assess the statistical significance of anomalies in a composite compared to the climatological values and the disparity between two composites. The statistical significance of the synergistic effect is also evaluated using bootstrap methods. In our analysis, we implement the bootstrap methods through a resampling process. Specifically, we resample all the joint events and isolated events in the dataset 1000 times and examine the 10th and 90th percentiles of the resulting synthetic distribution to draw meaningful statistical inferences (Deser et al. 2017, 2018; Tang et al. 2023).

2.2.3 Rossby wave ray flux (WRF)

To analyze the activity of stationary Rossby waves, we calculated the Rossby wave source (RWS) (Sardeshmukh and Hoskins, 1988):

$$RWS = -\zeta_a D - \overline{v_\chi} \cdot \nabla \zeta_a, \tag{4}$$

where ζ_a denotes absolute vorticity, D represents divergence, and $v_\chi$is the divergent wind. The RWS lies primarily in its contribution to vorticity changes, which can be decomposed into two terms: the vortex stretching (first term) and the advection of absolute vorticity (second term). For 200 hPa monthly mean wind, RWS intensity peak with strong convective outflow, horizontal divergent flow, pronounced vorticity gradients, and maximum intensity of the jet streams (Scaife e al. 2017).

The Takaya and Nakamura (TN) wave activity flux, which is applicable to both stationary and migratory quasi-geostrophic eddies within a zonally varying basic flow, serves as a robust diagnostic tool for identifying where a packet is emitted and absorbed (Takaya and Nakamura 2001). This specific wave activity flux is derived from the quasi-geostrophic potential vorticity equation, which is linearized with respect to a steady, non-uniform basic-state wind field.

The far-field atmospheric response to large-scale forcing in the atmosphere is dominated by external Rossby waves (Hoskins and Karoly 1981; Wallace and Gutzler 1981). Stationary Rossby wave ray is used to reflect the stationary planetary and Rossby wave energy propagation originating from local forcing (Hoskins and Ambrizzi 1993). Rossby wave ray tracing theory in a horizontally non-uniform basic flow enables the determination of trajectories of the stationary Rossby wave energy in both tropical and extratropical regions under observed wind conditions (Li and Li 2012; Li et al. 2015, 2019a, 2021; Zhao et al. 2015, 2019). Building upon the existing Rossby wave ray tracing theories in horizontally nonuniform basic flows mentioned above, Yang and Li (2025) introduced a new concept of horizontal Rossby WRF (the Li-Yang WRF for short) to diagnose local activity and propagation direction of Rossby wave energy. The Li-Yang WRF is calculated to represent the flow amount of wave rays passing through a unit grid area per unit time (Yang and Li 2025) as follows

$$F_{WR} = \frac{1}{S_\varphi} \iint_{S_\varphi} \boldsymbol{V}_R dS_\varphi = \left(\mathrm{U}_R \mathbf{i} + \mathrm{V}_R \mathbf{j}\right), \tag{5}$$

where S_φ indicate the area element of the grid integral,

$$\mathrm{U}_R = \sum_{i=1}^{n} a \cos\varphi_i \frac{\Delta\lambda_{Ri}}{\Delta t}, \tag{6}$$

$$\mathrm{V}_R = \sum_{i=1}^{n} a \frac{\Delta\varphi_{Ri}}{\Delta t}, \tag{7}$$

where a is the radius of the earth, φ denotes the latitude, $\Delta\lambda_{Ri}$ and $\Delta\varphi_{Ri}$ (i=1, 2, …, n) represent the longitude and latitude distances of the wave ray trajectory passing through the given small grid, respectively. Δt represents the duration of the period for the ray passing through the given small grid with a horizontal resolution of 5° × 5° (latitude × longitude). The unit of the Li-Yang WRF is m s^{-1}. The magnitude of the WRF denotes the strength of local Rossby wave activity, while its vectors indicate the direction of wave propagation.

3 Synergistic effect of AO⁻ and El Niño on winter precipitation over Southern China

Figure 1 presents the composite anomalies of winter (NDJF) precipitation during the individual and joint events of AO⁻ and El Niño, the linear superposition of precipitation anomalies from individual events of AO⁻ and El Niño, and the nonlinear component of precipitation anomalies from the joint events. Under both the individual events of AO⁻ and El Niño, the SCWP exhibits positive anomalies, with anomalies stronger during ENSO⁺\AO⁻ than during AO⁻\ENSO⁺, suggesting that El Niño exerts a greater influence than AO⁻ on SCWP (Fig. 1a, b). While both AO⁻ and El Niño independently enhance SCWP, their co-occurrence leads to substantially larger magnitudes and a broader spatial scale. Moreover, the probability of increased SCWP during joint events is 100% (Fig. 1g), which is significantly higher than in individual events, indicating that the simultaneous occurrence of both factors is more conducive to explaining the SCWP increase. In addition, no synergistic effects were found in the remaining three phase combinations between AO and ENSO, indicating that the combination of AO⁻ and El Niño holds significant explanatory meaning for the occurrence of strong positive anomalies in SCWP events.

Importantly, the precipitation anomalies in the joint events exceed the linear sum of the individual events. Further analysis shows that the magnitude of the nonlinear component is comparable to that of the linear component (Fig. 1f), implying that nonlinearity may play an important role in the synergistic effect of these two factors on SCWP. During winter, when the AO⁻ and El Niño coincide, the two indices exhibit a weak negative correlation (r=−0.14), which fails to pass the significance test at the 0.1 level. This suggests that AO and ENSO may be linearly independent of each other. In addition, the intensities of the AO and ENSO indices during joint events are not significantly different from those during individual events (Fig. 1h), indicating that the nonlinear response of SCWP to AO⁻ and El Niño in the joint events is not caused by stronger AO or ENSO

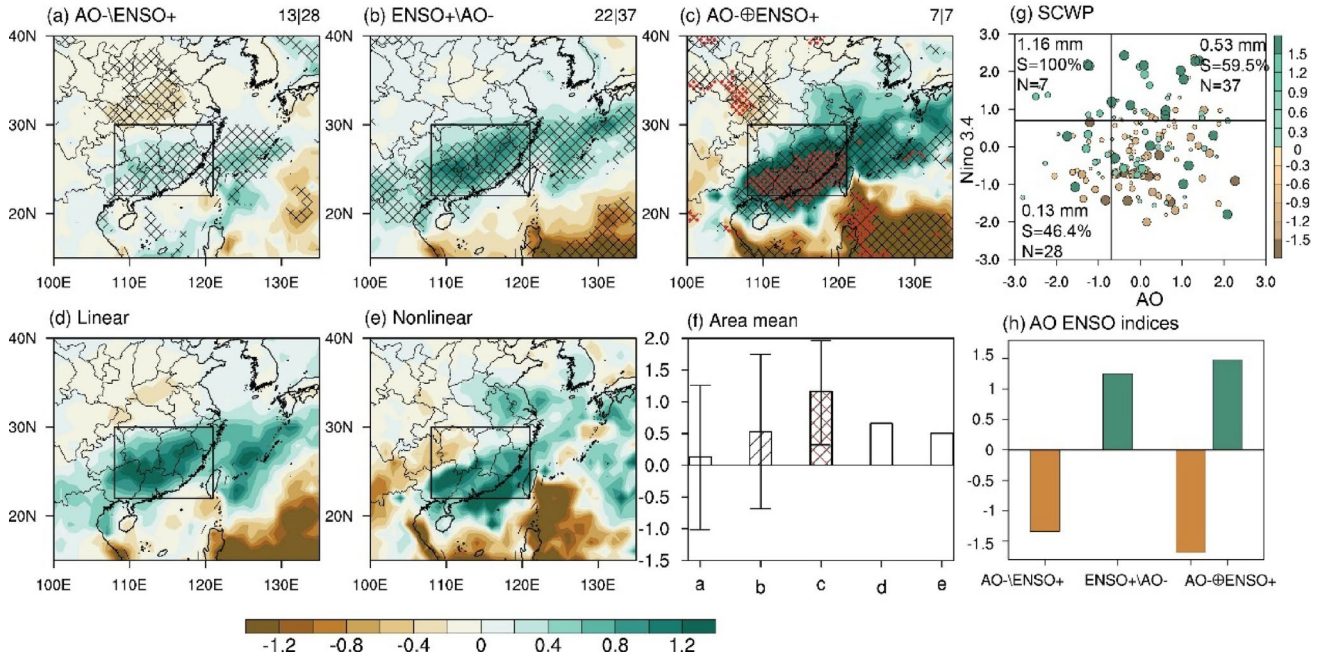

Fig. 1 Composite mean anomalies of winter (NDJF) precipitation: **a** $AO^-\backslash ENSO^+$, **b** $ENSO^+\backslash AO^-$, **c** $AO^- \oplus ENSO^+$, **d** linear superposition of **(a)** and **(b)**, **e** difference between **(c)** and **(d)**. Bars in **(f)** indicate area-mean precipitation within the boxed regions (22°N−30°N, 108°E−121°E) in **(a–e)**, and the letters "a" to "e" on the x-axis in **(f)** indicate SCWP in panels **(a)** to **(e)**, respectively. **(g)** Synergistic scatter plot of SCWP for AO and Niño 3.4 indices, the "S" in **(g)** denotes the occurrence frequency of positive precipitation anomalies across individual and joint events, and the "N" in **(g)** indicates the number of composite samples for each event type. **(h)** Composites of AO and Niño 3.4 indices under individual and joint events of AO^- and ENSO. Crossed areas in **(a-c)** are significant at the 90% confidence level. Red dotted areas in **(c)** indicate precipitation in **(c)** are significantly stronger than those in **(a)** and **(b)**. Black slash bars in **(f)** indicate composites to mean state are significant at the 90% confidence level, and red slash bar in **(f)** indicate SCWP in **(c)** is significantly stronger than that in **(a)**. The line variation over the bar in **(f)** indicates standard deviation

intensities. This further demonstrates potential involvement of more complex nonlinear processes.

To further understand the relationship between AO, ENSO and SCWP, we explore the local covariance of AO, ENSO with SCWP during the individual and joint events of AO^- and El Niño (Fig. 2). As shown in Fig. 2, the local covariance of negative AO and Niño3.4 indices with precipitation is similar to composition results shown in Fig. 1, suggesting that the local covariance can reflect the relationship between AO, ENSO and SCWP. Notably, during individual events, the Niño3.4 index exhibits a greater influence on SCWP than the AO does. However, the local covariance between the AO and SCWP is slightly (but not significantly) stronger than that between Niño3.4 index and SCWP. This pattern aligns with the observation that the AO index during $AO^- \oplus ENSO^+$ is non-significantly stronger than during $AO^-\backslash ENSO^+$. This is essential for understanding their synergistic mechanism. The precipitation anomalies under $AO^- \oplus ENSO^+$ are affected by both AO^- and El Niño, while the local covariance of both negative AO and Niño 3.4 indices with precipitation is significantly stronger than that of the individual events (Fig. 2c, d), reflecting the fact that both AO^- and El Niño contribute positively to precipitation anomalies. Rather than offsetting each other, the concurrent effects of AO^- and El Niño on precipitation show significant amplification, indicating a distinct synergistic effect between AO^-, El Niño and SCWP.

4 Synergistic effect of AO^- and El Niño on circulation

Figure 3 presents the zonal-mean-removed 500-hPa circulation anomalies during individual AO^- events, individual El Niño events, and their concurrent occurrences. When AO^- occur without El Niño, the dipole circulation anomaly in the North Atlantic is stronger than that in the North Pacific, and an anomalous northwest-southeast (positive–negative-positive–negative) circulation structure appears from the North Atlantic to southern China (Fig. 3a). When El Niño occur without AO^-, a Pacific-North American (PNA)-like teleconnection pattern emerges across the Pacific and North American sectors, while a negative NAO-like circulation pattern dominates the North Atlantic region. This corresponds to non-significantly stronger AO indices during joint events than $AO^-\backslash ENSO^+$ (Fig. 1h), as results from previous studies that El Niño favor a stronger negative phase of NAO (e.g., Li and Lau. 2012; Ayarzagüena

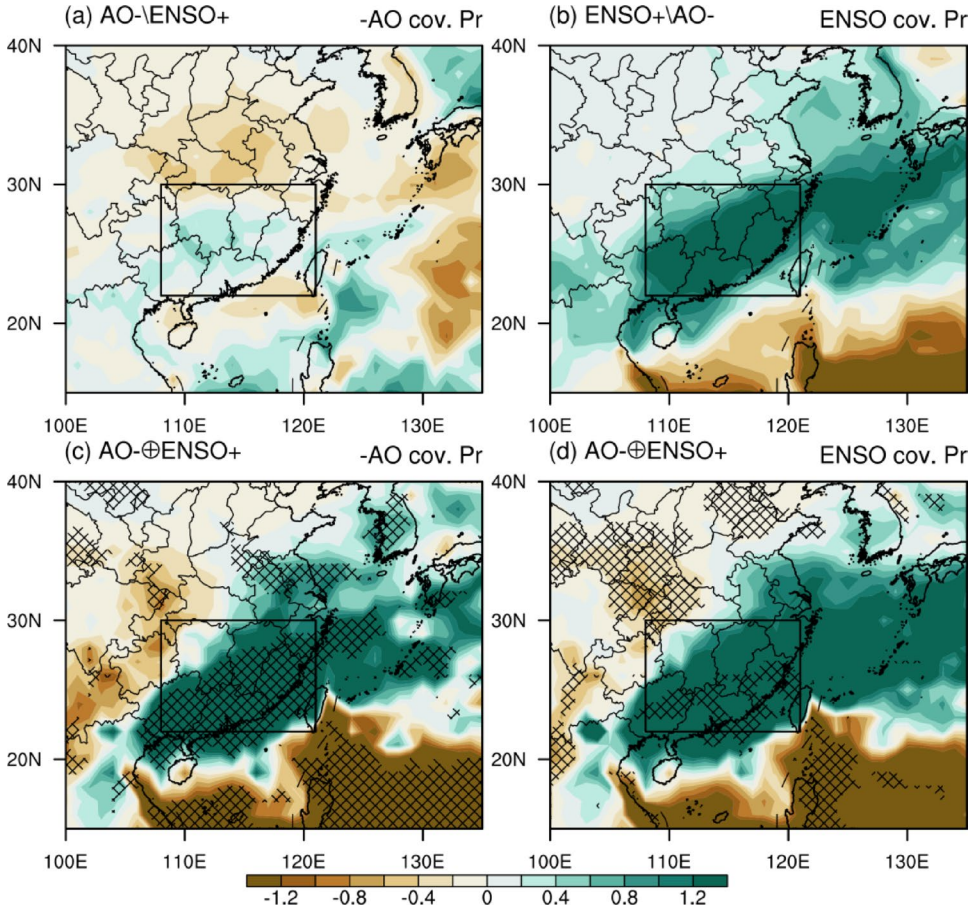

Fig. 2 Local covariance between winter precipitation anomalies and indices of −AO (left panels) and Niño 3.4 (right panels) under **a** $AO^{-}\backslash ENSO^{+}$, **b** $ENSO^{+}\backslash AO^{-}$, and **c, d** $AO^{-} \oplus ENSO^{+}$. The black crossed areas in **(c)** and **(d)** are significantly different from that in **(a)** and **(b)** at the 90% confidence level determined by bootstrap method, respectively

et al. 2018; King et al. 2018; Zhang et al. 2019; Chapman et al. 2021). This helps to explain the stronger relationship between AO and SCWP than that between Niño3.4 and SCWP during $AO^{-} \oplus ENSO^{+}$ (Fig. 2c, d). This large-scale atmospheric configuration further accompanies with alternating negative and positive circulation anomalies from the mid-latitude Atlantic to East Asia, with a weak anomalous low-pressure system over southern China (Fig. 3b). The large-scale geopotential height anomalies in both the tropics and Northern hemisphere during individual AO^{-} and El Niño events respectively exhibit spatially phase-locked patterns. These patterns manifest as coherent in-phase linear superposition of anomalies, resulting in amplified wave trains with uniformly signed anomalies extending from the North Pacific westward to East Asia (Fig. 3d). The mid-latitude negative geopotential height anomalies resulting from this linear superposition are particularly prominent over East Asia, the North Pacific, and the North Atlantic. When AO^{-} and El Niño co-occur, the resulting circulation anomalies significantly intensify beyond each of their individual effects (Fig. 3c). The observed amplitude surpasses what would be expected from simple linear superposition, demonstrating a notable nonlinear enhancement effect. This nonlinear response in the mid-latitudes displays a zonally inhomogeneous characteristic, characterized by an anomalous enhancement of the Aleutian low, enhanced positive geopotential height over western North America, and a deepened anomalous low over the eastern North Atlantic. Subsequently, the atmospheric circulation pattern splits into two pathways: one in the mid-latitudes and the other in the tropics. This nonlinearly amplified circulation closely resembles that observed during $AO^{-} \oplus ENSO^{+}$ events. Notably, the positive geopotential height anomalies over the tropical northwestern Pacific (TNWP) exhibits a pronounced nonlinear enhancement (Fig. 3e, g), creating favorable conditions for the development of southerly wind anomalies across southern China.

The far-field atmospheric response to large-scale forcing in the atmosphere is dominated by external Rossby waves (Hoskins and Karoly 1981; Wallace and Gutzler 1981; Held 2001). To further investigate the synergistic effects of the AO^{-} and El Niño on circulation from the perspective of Rossby wave activity, we perform a composite analysis of the RWS (Fig. 4). It is found that the AO^{-} and El Niño exhibit a significant synergistic effect on the negative anomalies of RWS in the mid-latitude Atlantic (Fig. 4a–c). Furthermore, the Eurasian subtropical westerly jet and midlatitude westerly jet are stronger during joint events

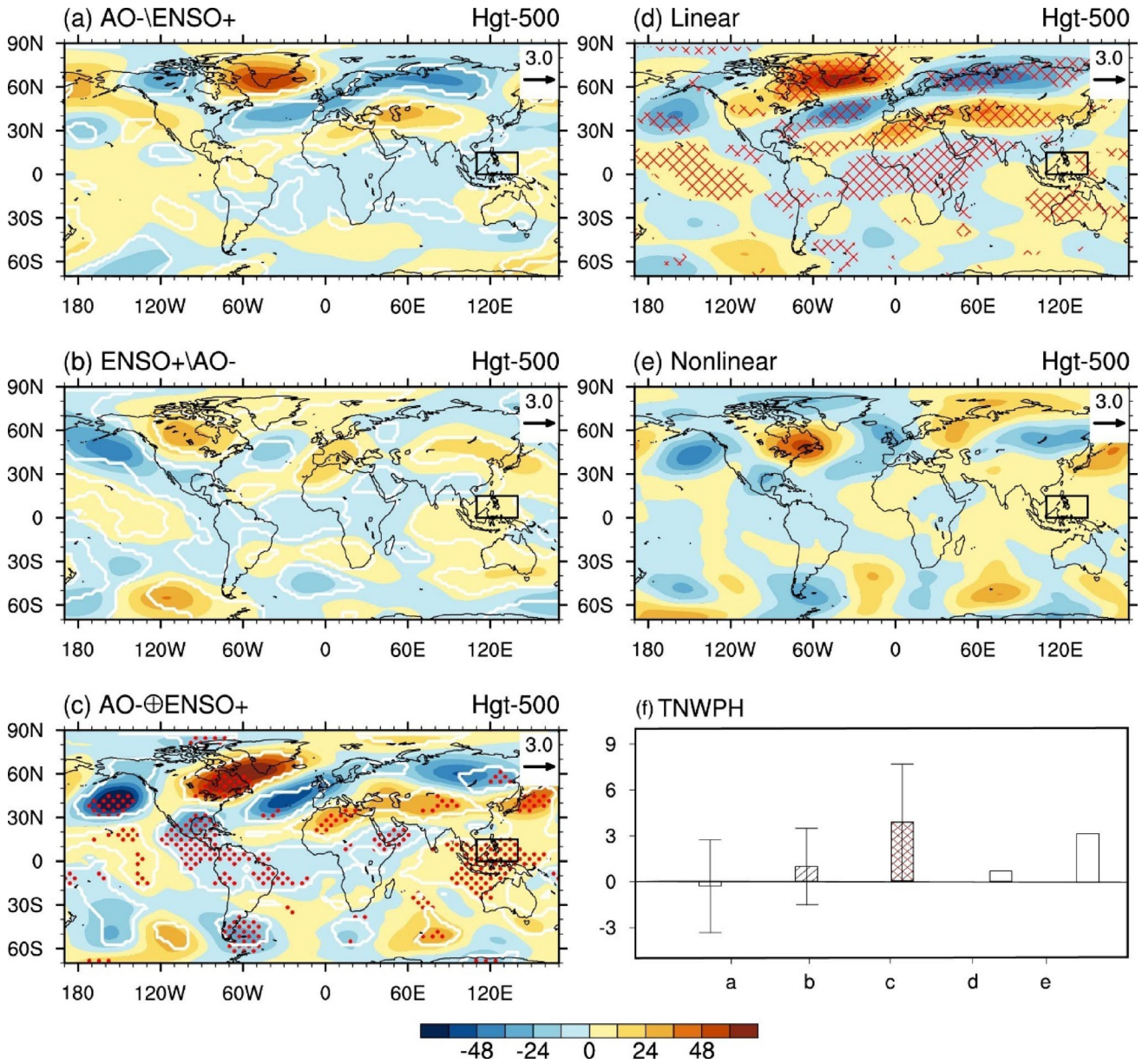

Fig. 3 As in Fig.1 **(a–e)**, but for NDJF geopotential height anomalies (zonal-mean removed; shading; gpm) at 500 hPa. **(f)** The area-averaged geopotential height anomalies over tropical northwestern Pacific (0°–15°N, 110°E–140°E) in **(a)** to **(e)**. The white contour lines indicate significant values at the 90% confidence level based on the Bootstrap method. The red crossed areas in **(d)** denote regions where the signs of anomalies (positive/negative) are consistent between **(a)** and **(b)**

than those during individual events (Fig. 4a–d). The intensification of the westerly waveguide establishes favorable dynamical conditions for the propagation of Rossby wave energy (Li et al. 2012). The RWS associated with El Niño is set in the upper troposphere over the equatorial Pacific (5°S–5°N, 170°E–155°W), where strong divergence prevails (Fig. 4b, c), as conducted in Tang et al. (2023). During $ENSO^{+}\backslash AO^{-}$ events, Rossby waves generated in the equatorial Pacific exhibit northward propagation through two primary waveguide channels: the polar front and subtropical jets. The northern branch of the Rossby wave triggered over the tropical Pacific first propagates northward toward the North Pacific, leading to an intensification of the Aleutian Low. It then propagates downstream along the subpolar jet stream toward East Asia. This teleconnection pathway is hereafter referred to as the North Pacific–East Asia (NPEA) teleconnection. Upon reaching western Europe and northern Africa, the Rossby wave energy separates into two distinct branches: (i) a continuation along the polar front jet to southern China, and (ii) a trans-equatorial branch that crosses into the Southern Hemisphere through the North African channel (Li et al. 2019a), subsequently splitting

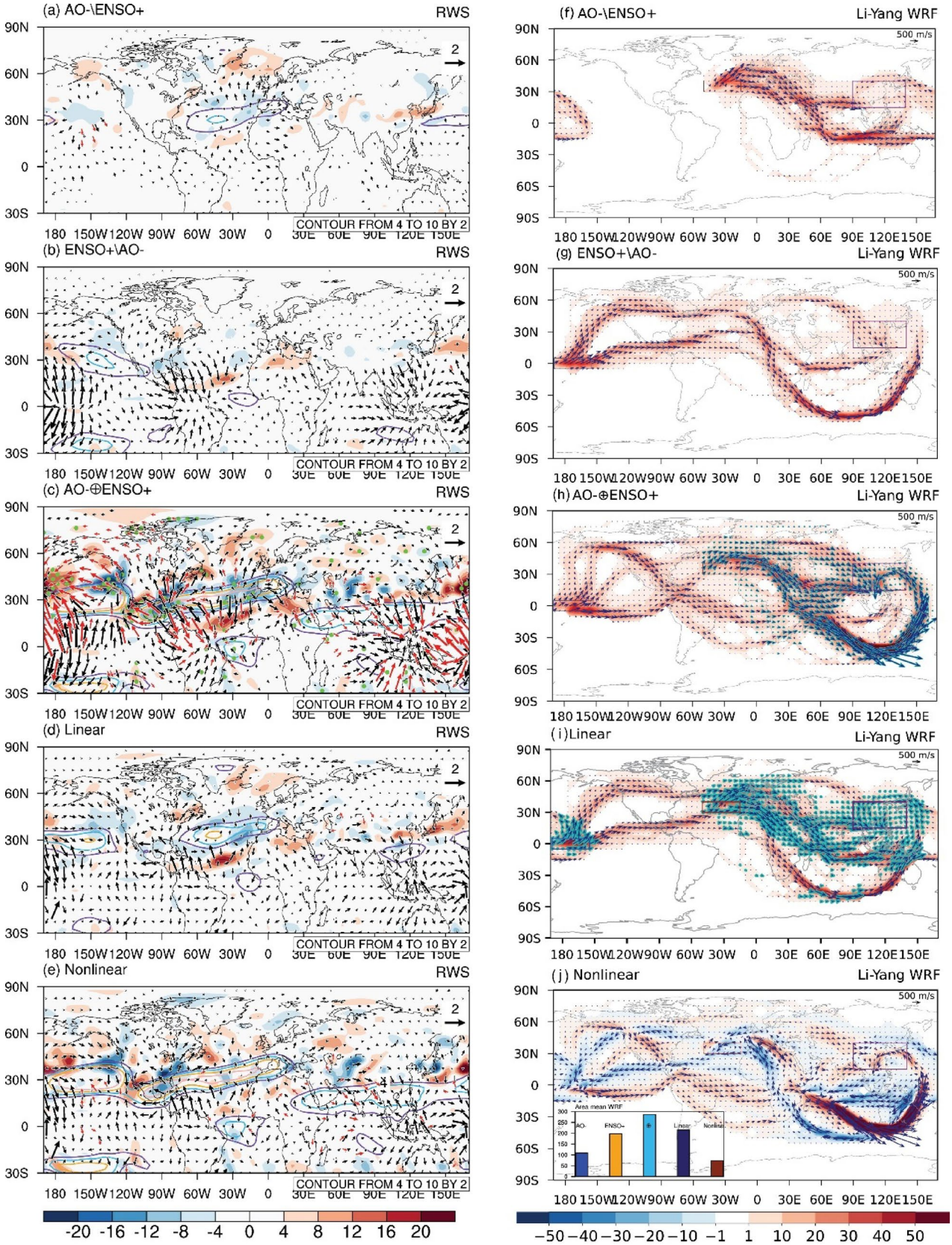
(a) AO-\ENSO+
RWS
(b) ENSO+\AO-
RWS
(c) AO-⊕ENSO+
RWS
(d) Linear
RWS
(e) Nonlinear
RWS
CONTOUR FROM 4 TO 10 BY 2
-20 -16 -12 -8 -4 0 4 8 12 16 20
(f) AO-\ENSO+
Li-Yang WRF
(g) ENSO+\AO-
Li-Yang WRF
(h) AO-⊕ENSO+
Li-Yang WRF
(i)Linear
Li-Yang WRF
(j) Nonlinear
Li-Yang WRF
500 m/s
Area mean WRF
AO-
ENSO-
+
Linear
Nonlinear
−50 −40 −30 −20 −10 −1 1 10 20 30 40 50

Fig. 4 (Left) Composite 200-hPa anomalies of RWS (shading; 10^{-10} s^{-2}), anomalous divergent wind (vector; m s^{-1}), and 200-hPa zonal wind (m s^{-1} shown contours). (Right) Li-Yang WRF (vector; m s^{-1}) and its magnitude (shading; m s^{-1}) initiated from tropical Pacific (5°S–5°N, 170°E–155°W; northern pathway) and North Atlantic (30°N–40°N, 50°W–15°W), and the evolution of total wavenumber initiated with zonal wavenumber 3–5. The arrows and green dotted areas in left panels indicate values in **(c)** are significantly stronger than those in **(a)** and **(b)**. Black vectors in left panel indicate divergent winds are significant at the 90% confidence level based on bootstrap, and only vectors with magnitudes exceeding 0.5 m s^{-1} are displayed. The green arrows in **(i)** indicate that the Li-Yang WRF in **(f)** and **(g)** superimpose in this grid cell. The cyan arrows in **(j)** indicate that the Li-Yang WRF of Rossby wave excited from the equatorial Pacific and North Atlantic superimpose in this grid cell. The bar chat in the bottom-left corner of **(j)** denotes the area mean values of WRF within the boxed region (15°N − 40°N, 90°E − 140°E) shown in **(f–j)**

into two pathways following counterclockwise trajectories through the tropical and subtropical Indian Ocean before recurving to influence East Asia circulation (Fig. 4f). The WRF pathways excited from tropical Pacific identified in this study further support the established understanding that ENSO can induce global teleconnections (Trenberth et al. 1998; Alexander et al. 2002). The RWS associated with AO^- is set in the North Atlantic (30°N–40°N, 50°W–15°W) where upper-level divergent winds and strong westerly jet stream prevail. This region is selected because the circulation anomalies over the North Atlantic during AO^-\ $ENSO^+$ events are more pronounced than those over the North Pacific (Fig. 3a), making it the dominant RWS for downstream wave propagation towards East Asia. During AO^-\$ENSO^+$ events, Rossby waves excited over the North Atlantic propagate via two distinct pathways to East Asia: (1) Along the Asian-African subtropical jet stream, resembling the South Eurasian (SEA) teleconnection (Xu et al. 2013); and (2) A trans-equatorial route extending from Europe across the Red Sea and Indian Ocean into the tropical Southern Hemisphere, subsequently reaching East Asia via a counterclockwise propagation trajectory.

The NPEA teleconnection associated with El Niño, which extends across the North Atlantic (Fig. 4f), indicates that El Niño can remotely influence atmospheric circulation in the North Atlantic region (Zhang et al. 2019; Tang et al. 2023). This corresponds to an anomaly weak NAO-like circulation North Atlantic region during $ENSO^+$\AO^- events (Fig. 3b). Over the North Atlantic region, the midlatitude cyclonic circulation associated with El Niño exhibits constructive interference with the AO^--related cyclonic anomaly (Fig. 3c). This induces relatively stronger RWS in the subtropical and midlatitude North Atlantic during $AO^- \oplus ENSO^+$ events (Fig. 4c), thereby favoring the stronger Li-Yang WRF of Rossby waves from North Atlantic to East Asia. Notably, AO^- and El Niño jointly modulates the circulation anomaly over the North Pacific, the presence of the AO^- compared to its absence alters the path of Rossby waves originating from the tropical Pacific (Fig. 4g, h). In addition, the Li-Yang WRF associated with El Niño superimposed with the AO^--related eastward Li-Yang WRF from Europe to East Asia (Fig. 4h) along three pathways from Europe to East Asia: the midlatitude pathway, subtropical westerly jet stream pathway and cross equatorial pathway (Fig. 4h). The resulting Li-Yang WRF during $AO^- \oplus ENSO^+$ events is significantly stronger than those during individual events and exceeds the linear superposition of the individual contributions across all three pathways (Fig. 4j). For the sake of brevity, the cross-equatorial propagation of Rossby wave energy, which initialed in the North Atlantic propagates through the Indian Ocean, and ultimately reaches East Asia is referred to as the North Atlantic-Indian Ocean-East Asia (NIE) teleconnection. Specifically, the intensification of subtropical westerly anomalies over South and East Asia facilitates the development the SEA teleconnection, while midlatitude westerly anomalies over Eurasia support the NPEA teleconnection. Furthermore, intensification of Asian-African subtropical westerly jet (AASWJ) stream promotes the cross-equatorial wave propagation near the Red Sea, which is dynamically associated with the NIE teleconnection (Fig. 4c, h). The intensification of three Li-Yang WRF pathways corresponds to the amplified anomalous wave train from the midlatitude North Pacific to the TNWP and Southern China (Fig. 3f, h). Although the nonlinear component of Li-Yang WRF arriving at East Asia (73.75 m/s) accounts for approximately one-quarter of the total Li-Yang WRF (215.61 m/s) during the joint events, its contribution to the nonlinear amplification of the atmospheric circulation is non-negligible. This amplification causes the actual impact during co-occurring AO^- and $ENSO^+$ events to significantly exceed the simple linear superposition of their independent influences, thereby achieving a genuinely nonlinear synergistic effect.

The intensified three pathways of Li-Yang WRF within the nonlinear term are spatially aligned with the linear superposition components of AO^- and $ENSO^+$. This suggests the nonlinear term does not represent independent wave source, but rather emerges from the in-phase superposition of the linear wave trains originated from the tropical Pacific and North Atlantic. When those two linear wave trains achieve spatial phase alignment downstream of the North Atlantic (Figs. 3d, 4h), they induce a pronounced enhancement of circulation anomalies (Fig. 3c) and a strengthening of the jet stream (Fig. 4c), thereby further facilitating its propagation downstream. In this progress, atmospheric internal dynamics—primarily wave-mean flow interaction may play a key role in the nonlinear term of Rossby wave train.

Based on the above analysis, the AO^- and El Niño synergistically enhance the upstream wave activity propagating to the Eurasian region. Similar characteristics are evident in the TN wave activity flux, where the joint events amplify

the co-enhanced wave activity propagating from the Atlantic to the entrance region of the AASWJ. The combined effect between AO⁻ and El Niño generates an enhancement of North Atlantic subtropical westerly jet during joint events, exceeding the linear superposition of the individual forcing responses (Fig. 5d–e). The TN-wave activity flux indicate that the kinetic energy of the North Atlantic subtropical westerly jet can diverges into the AASWJ entrance region. To quantify the dynamic link between this wave energy and the AASWJ, we conducted a correlation analysis between the wave activity in the AASWJ entrance region (20°N–30°N, 0°–30°E) and kinetic energy. The results show that enhanced wave energy convergence in this region corresponds to increased kinetic energy across the AASWJ (Fig. 5a–c), suggesting that the intensified wave energy convergence in the inlet region of AASWJ can provide the dynamic forcing that accelerates and intensifies the AASWJ. The strengthened AASWJ, in turn, acts as a more efficient waveguide, further promoting the downstream propagation of the Rossby wave energy along the AASWJ. Ultimately, the amplified wave train propagates farther downstream, where its energy dispersion and vorticity forcing modulate the downstream atmospheric circulation. Correspondingly, during joint events, the East Asian subtropical westerly jet stream and the negative anomalous westerlies to its north exhibit significant nonlinear intensification, exceeding their linear superposition (Fig. 5e). These circulation anomalies correspond to markedly enhanced anticyclone anomaly over

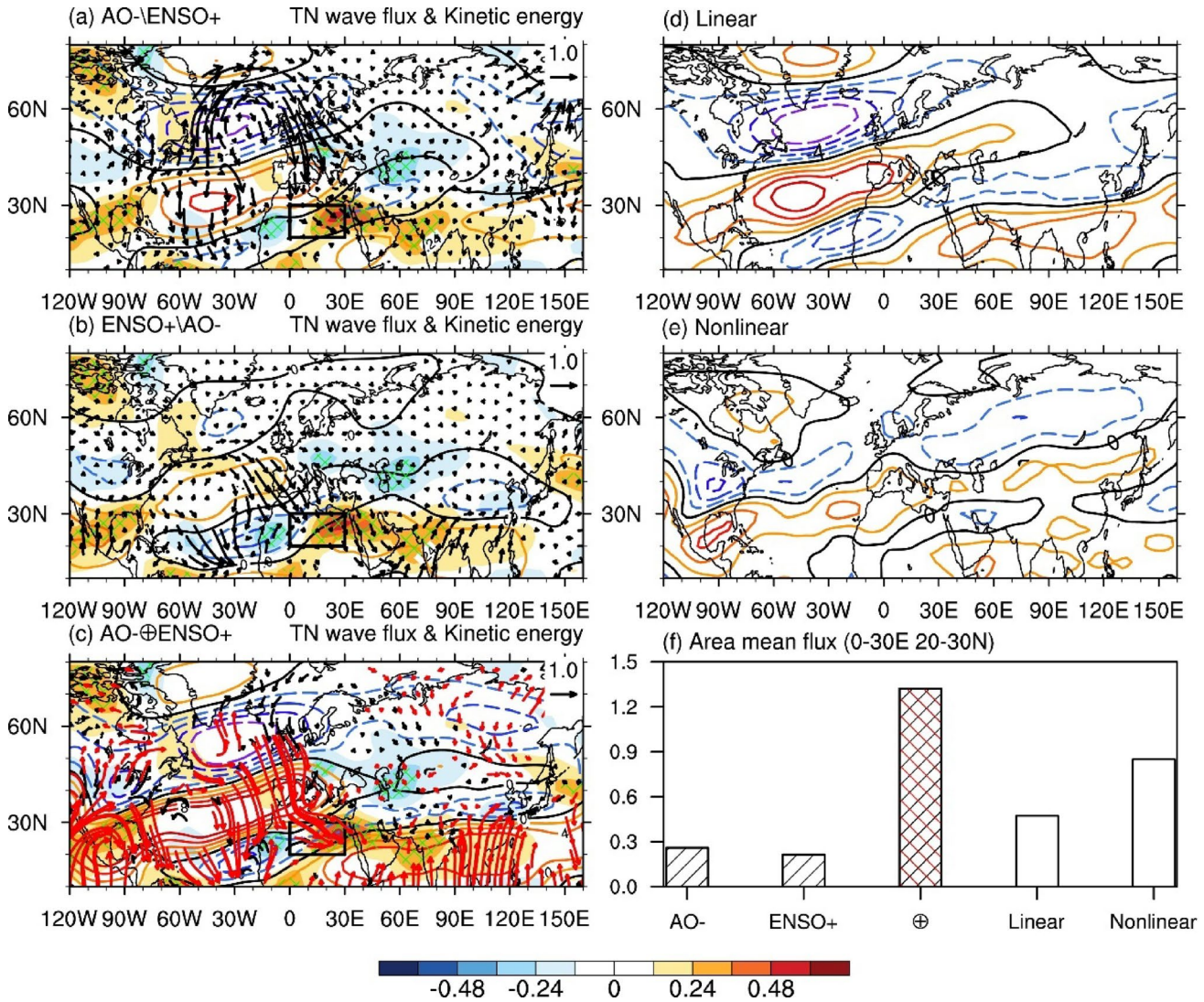

Fig. 5 Composite anomalies of NDJF wave activity flux (arrows; $m^2 s^{-2}$) and zonal wind anomaly (contours; m s^{-1}), along with correlation coefficients between the area-mean wave fluxes within the black boxed region and kinetic energy (shading; m s^{-1}) at 200 hPa (left panel). Red arrows in **(c)** denote regions where the values are significantly greater than those in **(a)** and **(b)**. Green crossed areas in **(a–c)** indicate correlation coefficients are significant at the 90% confident level. **(f)** is the same as in Fig. 3f, but for area mean wave flux within the black boxed region (20°N–30°N, 0°–30°E)

TNWP and cyclonic circulation over Southern China, which in turn influences the SCWP. This is similar with the results from Wei and Zhang (2021) that the kinetic energy anomalies in the inlet region of AASWJ can downward along AASWJ, and modulate TNWP high.

5 Synergistic effect of AO⁻ and El Niño on SCWP formation

To investigate the mechanisms of SCWP formation under AO⁻ and El Niño conditions, Fig. 6 presents the water vapor transport at 850 hPa under individual and joint events of AO⁻ and El Niño. During AO⁻\ENSO⁺ events, southern China receives enhanced moisture transport via southwesterly flow originating from the Indian Ocean (Fig. 6a). During ENSO⁺\AO⁻ events, the TNWP anticyclone facilitates intensified southwesterly warm-moist flow from both the Indian Ocean and South China Sea toward southern China (Fig. 6b). Notably, the TNWP anticyclone strengthens significantly during co-occurring AO⁻ and El Niño events compared to isolated cases, amplifying moisture flux to southern China (Fig. 6c). The moisture reaching southern China under joint events exceeds the linear superposition of individual events, with nonlinear components contributing approximately half of the linear superposition components (Fig. 6d–f). This nonlinear amplification of anticyclonic moisture transport under the combined effect of AO⁻ and El Niño corresponds to the enhancement of TNWP high anomaly (Fig. 3d, f).

The moisture transport coupling with ascending motion is favorable for precipitation generation. Figure 7 displays anomalous composites of meridional-vertical circulation (zonally averaged across 105°E–130°E, 5°S–55°N) over East Asia during individual and joint events of AO⁻ and El Niño. During AO⁻\ENSO⁺ events, weak anomalous subsidence occurs near the equator, which then diverges northward, resulting in modest ascending motion in the lower troposphere around 25°N and forming a weak localized negative Hadley circulation anomaly (Fig. 7a). During ENSO⁺\AO⁻ individual events, this negative Hadley cell anomaly intensifies substantially, with whole-layer ascending motions emerging between 20°N–40°N that spatially align with precipitation anomalies (Fig. 1a, b). When AO⁻ and El Niño co-occur, the enhanced TNWP anticyclone is accompanied by significantly intensified subsidence, along with low-level divergence that subsequently converges toward southern China, thereby causing enhanced ascending motion (Fig. 7c). Moreover, the low-level convergence and ascending motion over southern China, as well as the tropical subsidence in the joint events are markedly stronger than those in individual events, with the nonlinear component being comparable to the linear superposition (Fig. 7d, e). Therefore, AO⁻ and El Niño exert a significant synergistic effect on moisture transport, low-level convergence, and ascending motion over southern China, leading to a pronounced enhancement of SCWP.

However, how do the AO⁻ and El Niño synergistically influence the descending motion over the TNWP? We demonstrated that AO⁻ and El Niño synergistically enhance Rossby wave energy propagation downstream to Southern China (Figs. 4, 5). Building on this, we examined the relationship between this enhanced downstream wave activity and the large-scale circulation. The correlation map between

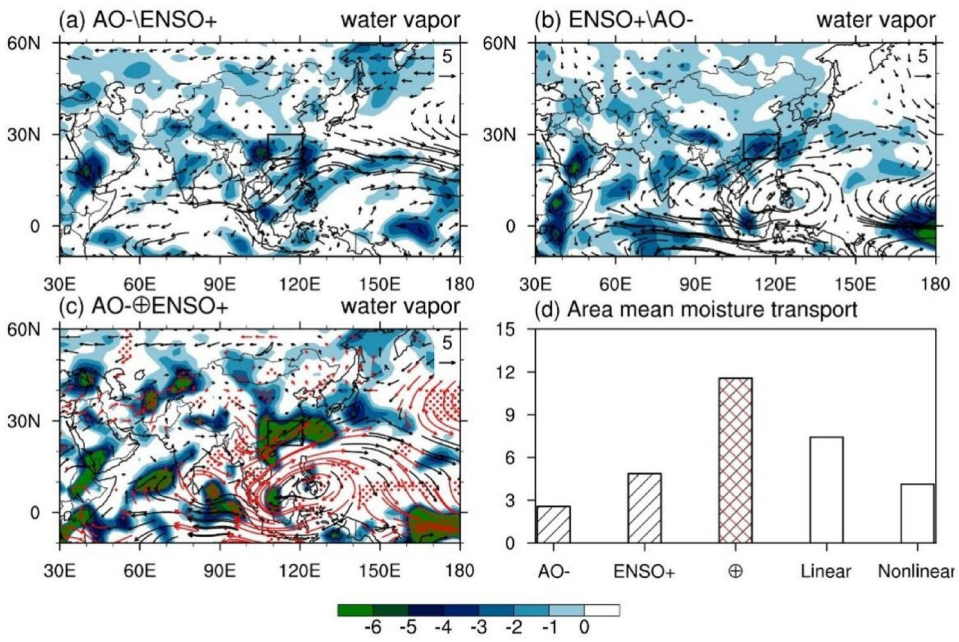

Fig. 6 Composite anomalies of NDJF water vapor transport at 850 hPa (vectors; g kg^{-1} m s^{-1}) and divergence ($\times -1$; shading; -10^{-6} g kg^{-1} s^{-1}). Red arrows and red dotted areas in **(c)** represent variables in **(c)** are significantly stronger than those in **(a)** and **(b)**. **(d)** is the same as in Fig. 3f, but for area mean moisture transport over Southern China

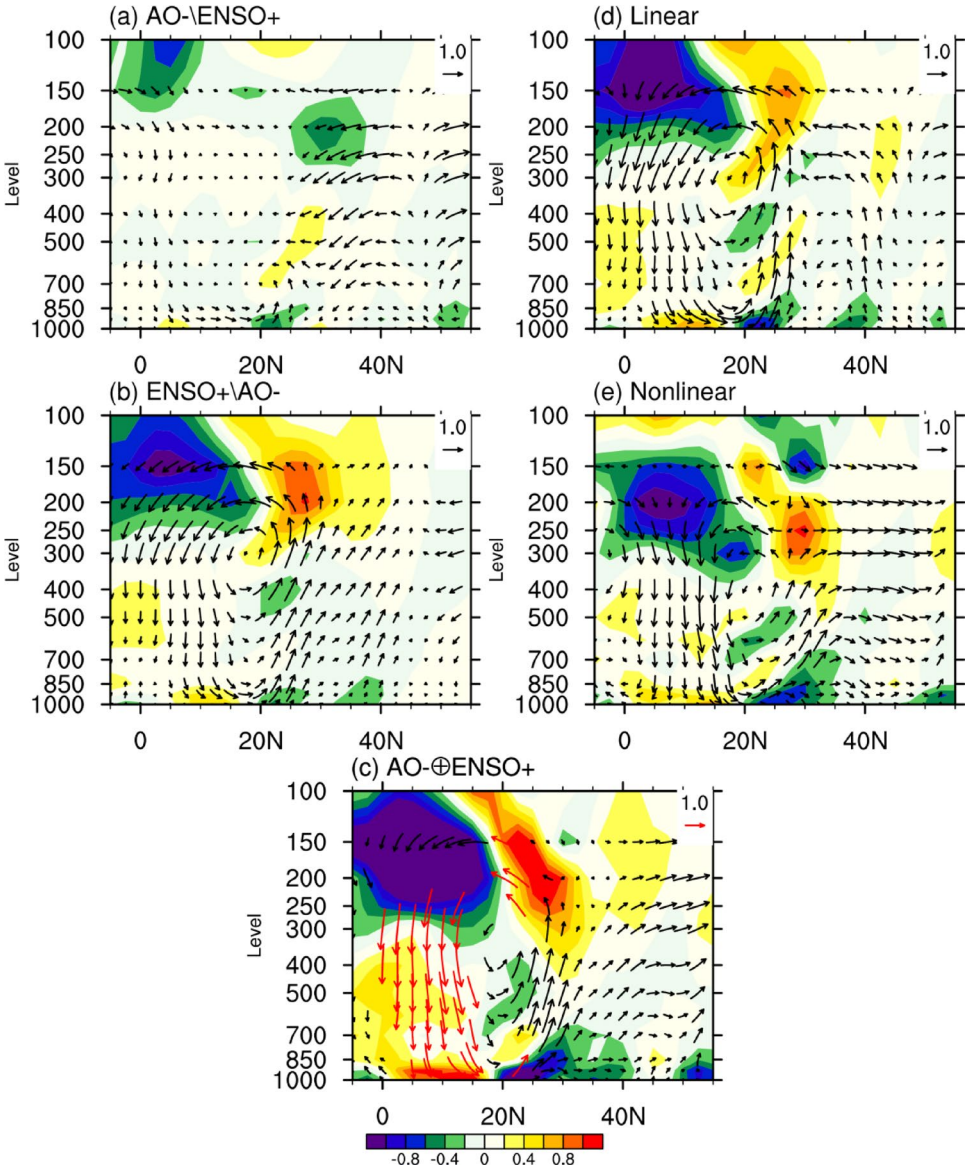

Fig. 7 Composite anomalies of meridional-vertical circulation $[u\mathbf{j} - \omega\mathbf{k}$; vectors; u in m s^{-1}; ω in hPa s$^{-1}]$ between 105°E−130°E and wind divergence (shading; 10^{-6} s.$^{-1}$). Red arrows in **(c)** denote regions where the values are significantly greater than those in **(a)** and **(b)**

regional wave activity flux over Southern China and geopotential height/vertical motion (Fig. 8a) reveals that anomalously strong wave activity over southern China coincides with significant positive geopotential height anomalies and enhanced subsidence over the TNWP. Moreover, the spatial distribution of WRF confirms that the TNWP is located downstream of the main energy propagation pathway of this synergistically enhanced Rossby wave train. Thus, the propagation of enhanced Rossby wave energy can exert a dynamic forcing on the atmosphere along its path, thereby influencing anomalous high geopotential height and subsidence in the TNWP region. Further analysis shows a close association between the anomalous TNWP high and the local subsidence, with a correlation coefficient of 0.57 (Fig. 8b). This supports that the nonlinearly enhanced descending motion in the TNWP can be attributed to the upstream reinforcement of Rossby wave energy propagation and the resulting intensification of the TNWP high.

Moreover, the descending motion in the TNWP is closely related to the Walker circulation. Figure 9 presents the composite anomalies of the Walker circulation under individual and joint events of AO$^-$ and El Niño. As shown in Fig. 9, El Niño induces upper-level divergence in the central equatorial Pacific while promoting upper-level convergence in the TNWP, thereby establishing an anomalous negative Walker circulation that results in subsidence in that region. Therefore, El Niño have an influence on the SCWP through two pathways: the Walker circulation and eastward propagation of Rossby waves. During ENSO$^+$\AO$^-$ events, anomalous ascending motion appears in the tropical eastern-central Pacific, whereas anomalous subsidence is evident around 120°E–150°E and near 60°W (Fig. 9b). The AO$^-$\ENSO$^+$

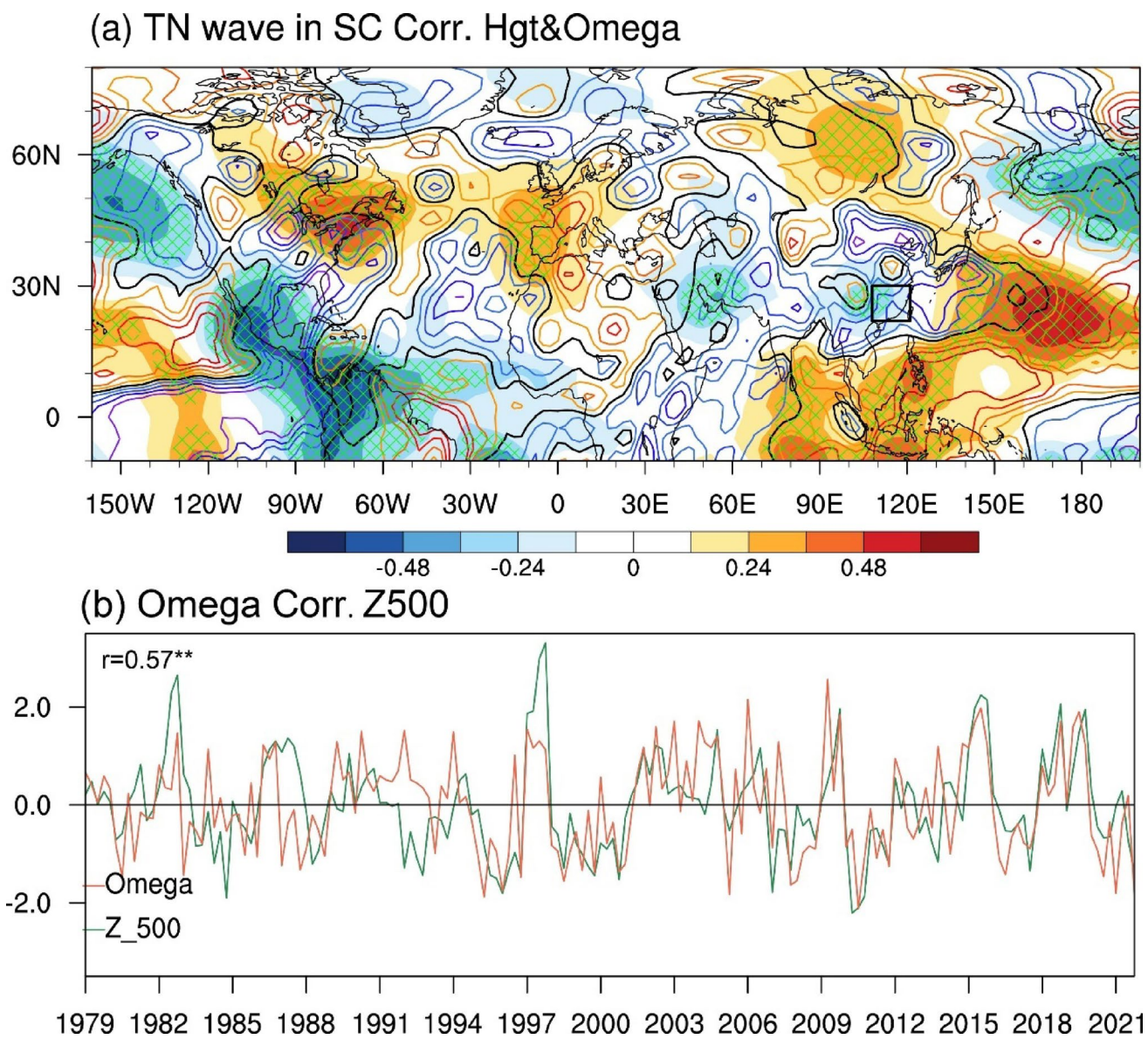

Fig. 8 **a** Correlation of TN wave activity flux over Southern China with 500 hPa geopotential height (shading) and vertical velocity (counter; positive indicates subsidence). **b** Standardized time series of area-averaged geopotential height (green) and vertical velocity (orange) at 500 hPa over the tropical northwestern Pacific (5°N−15°N, 105°E−130°E). Green crossed area in (**a**) denotes correlation significant at the 95% confidence level

events are characterized by relatively weak tropical vertical anomalies (Fig. 9a). During $AO^{-} \oplus ENSO^{+}$ joint events, the ascending motion in the tropical eastern-central Pacific is significantly enhanced particularly around 180°E, surpassing that observed in $ENSO^{+} \backslash AO^{-}$ events. Since the strength of El Nino events with AO^{-} is not significantly different with those without AO^{-} (Fig. 1h), the enhanced ascending motion in the tropical eastern-central Pacific is likely linked to the intensified descending motion over the TNWP via the Walker circulation.

6 Conclusions and discussion

While SCWP is known to respond to both AO^{-} and El Niño forcing, the potential synergistic effect between these climate modes remained unexplored before this study. Our analysis reveals a statistically significant synergistic amplification of SCWP under the combined effects of AO^{-} and El Niño, with precipitation intensity exceeding twice the magnitude observed during individual events and surpassing the linear superposition of individual event contributions. Crucially, joint events exhibit a 100% occurrence probability of positive SCWP anomalies, markedly higher than

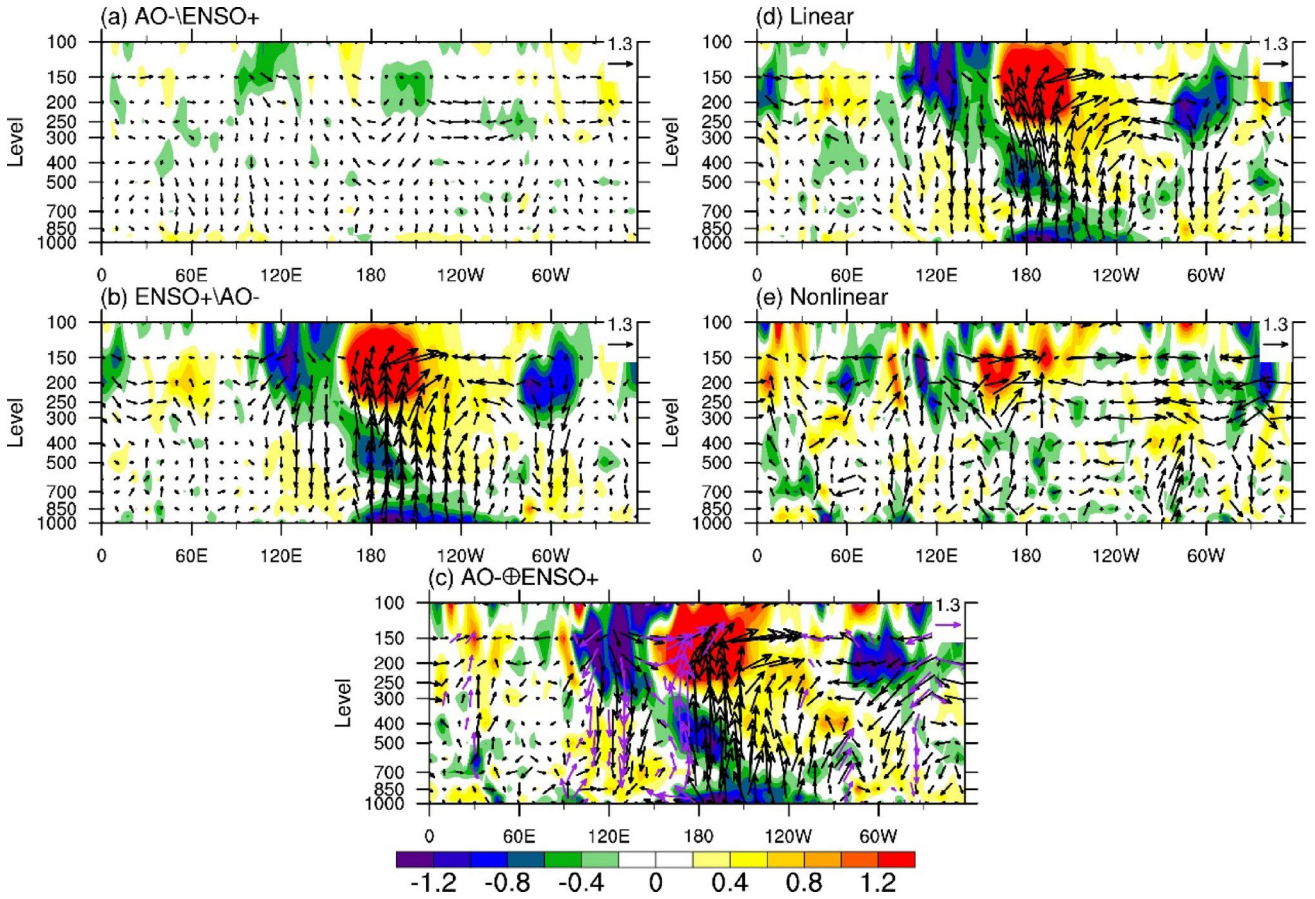

Fig. 9 Composite anomalies of zonal-vertical circulation [$v\mathbf{j} - \omega\mathbf{k}$; vectors; v in m s^{-1}; ω in Pa s^{-1}] between 5°S − 5°N and wind divergence (shading; 10^{-6} s^{-1}). Purple arrows in **(c)** denote regions where the values are significantly greater than those in **(a)** and **(b)**

probabilities associated with individual events. These findings establish that the co-occurrence of AO$^-$ and El Niño provides a comprehensive physical mechanism for explaining SCWP anomaly amplification, thereby advancing the understanding of SCWP variability.

Physical mechanisms reveal that both AO$^-$ and El Niño can excite eastward-propagating Rossby wave trains that influence East Asian circulations. Particularly, El Niño-induced Rossby waves exhibit an additional capacity to modulate North Atlantic circulation, favoring the negative phase of NAO$^-$-like circulation anomalies, which subsequently amplifies the AO$^-$related Rossby wave energy originating from the North Atlantic. Furthermore, during the joint events, the Rossby wave energy from both the tropical Pacific and North Atlantic demonstrates synergistic enhancement over the Eurasian continent to East Asia in three pathways, synergistically intensifying the TNWP high (Fig. 10). El Niño modulates SCWP through two distinct pathways: an eastward route via Rossby wave energy propagation and a westward route mediated by Walker circulation, both processes coexist and play important roles in influencing SCWP. This study reveals a significant nonlinear amplification of the TNWP high by combined AO$^-$ and El Niño forcing through Rossby wave energy propagation. The anomalous TNWP high is accompanied by descending motion in this region, which subsequently enhances low-level convergence and vertical ascent over southern China via meridional circulation (Fig. 10). In addition, the TNWP anticyclone enhances moisture transport toward southern China, resulting in increased SCWP.

We also selected AO$^-$ and El Niño events by applying an AO index threshold of 0.5-standard deviation and identifying El Niño years based on the ONI index, showing similar results (Fig. 11), and similarly results are found using the AO index from NOAA (Fig. 12; https://psl.noaa.gov/data/timeseries/month/DS/AO/), demonstrating the robust syne rgistic relationship between El Niño and AO$^-$ with SCWP.

The eastern-type El Niño has a stronger influence on SCWP (Xu et al. 2013). The differential synergistic impacts of central-Pacific and eastern-Pacific El Niño events with the AO$^-$ on the SCWP remain to be systematically investigated in the future. In this study, we have identified two atmospheric pathways through which El Niño influences SCWP: via the Walker circulation and through atmospheric

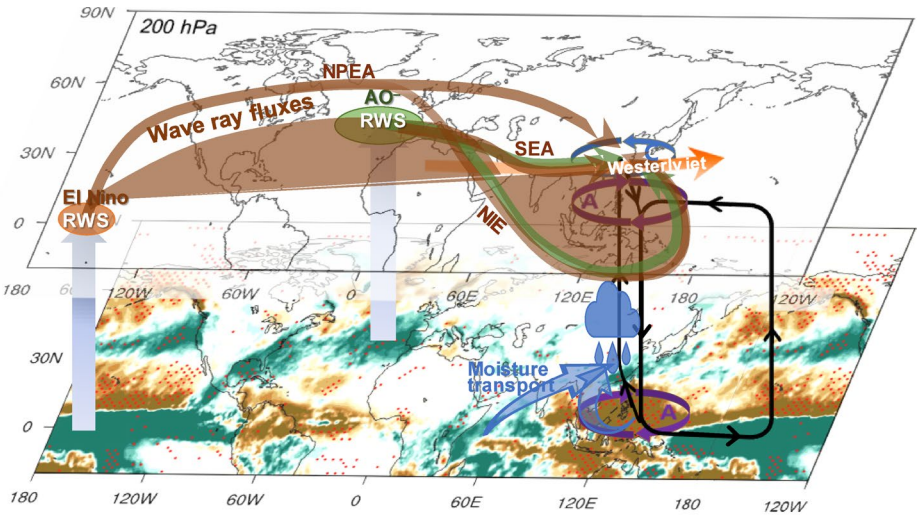

Fig. 10 Schematic diagram for synergistic effect of AO⁻ and El Niño on winter precipitation over the Southern China. Shading at the bottom indicates winter precipitation anomalies under the joint events of AO⁻ and El Niño

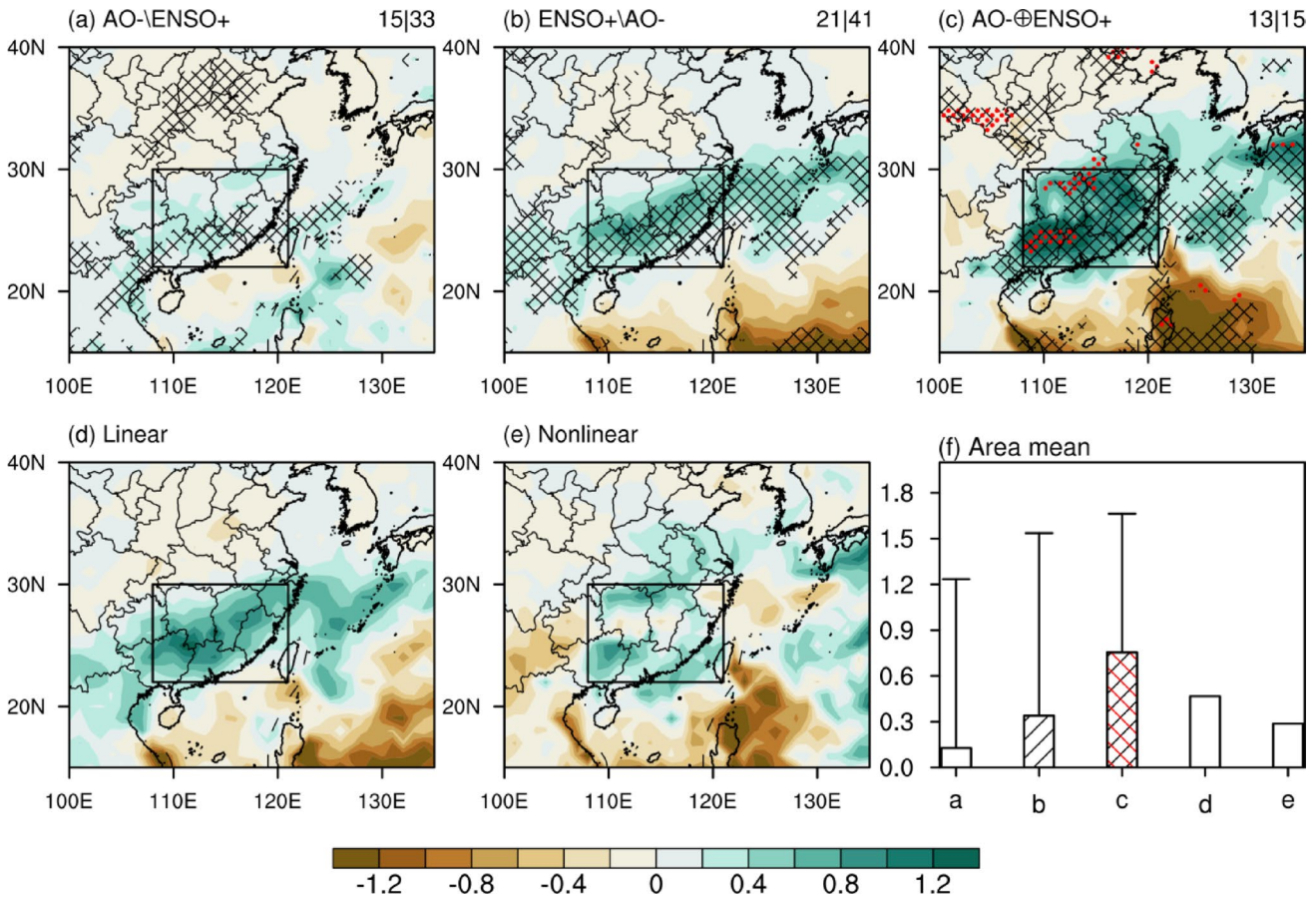

Fig. 11 Same as in Fig. 1a–f, but using a 0.5 standard deviation threshold

teleconnections. The relative importance between these two mechanisms remains to explore in future research. In addition, given that El Niño is commonly accompanied by Indian Ocean basin warming in winter, the potential role of the Indian Ocean on the synergistic effect between AO and El Niño is valuable to investigate in the future.

This study investigates the synergistic impacts of AO⁻ and El Niño on SCWP and elucidates their underlying mechanisms. Our findings conclusively demonstrate that AO⁻ and El Niño exert synergistic effect on SCWP intensity and occurrence through nonlinear effects. However, the precise magnitude of nonlinear components requires further

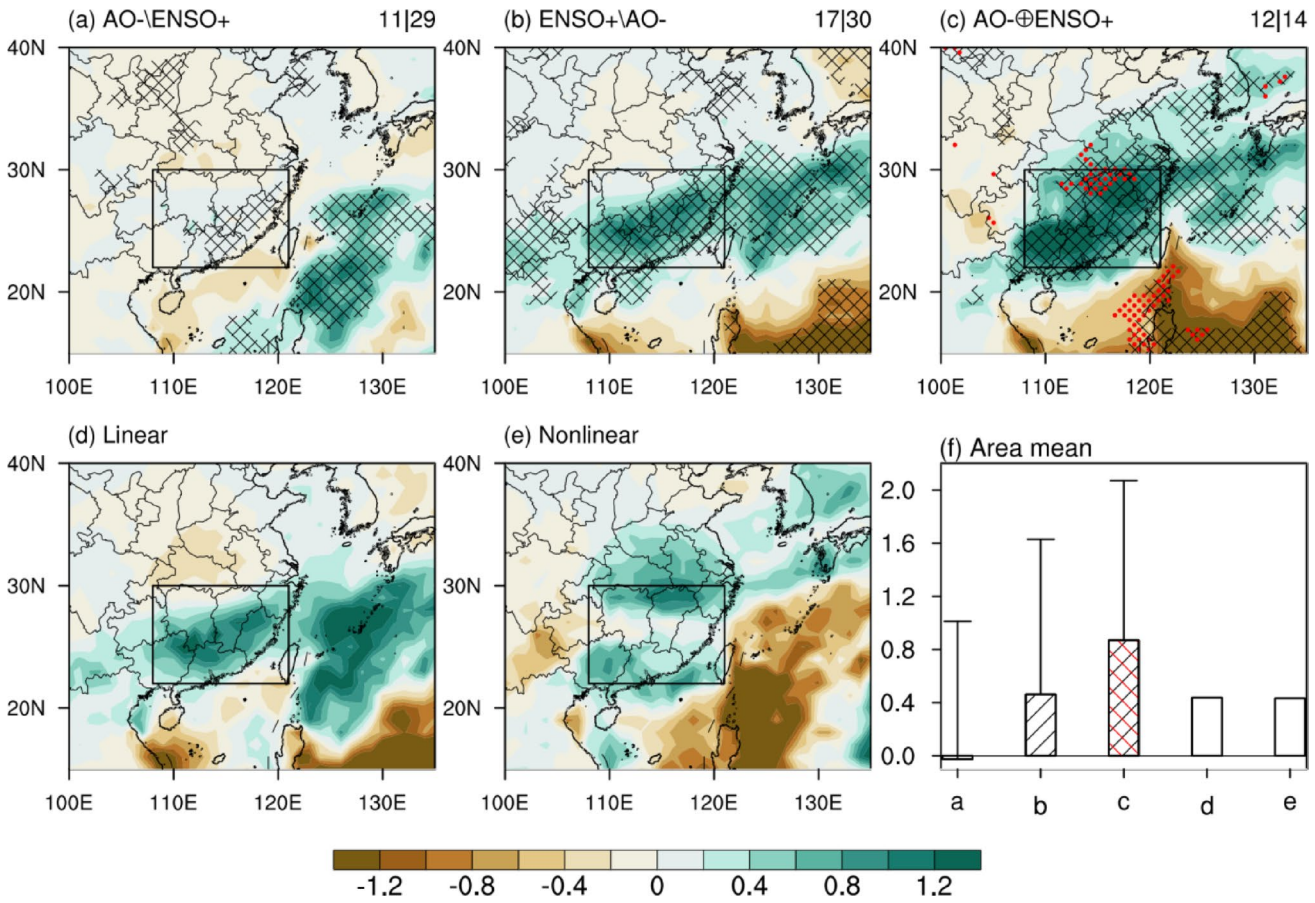

Fig. 12 As in Fig. 1a–f, but employing the AO index from NOAA

quantification through targeted numerical experiments in future work.

Acknowledgements We thank all the data providers. This work is supported by the National Natural Science Foundation of China (NSFC) Project (42288101 and 42130607), Fundamental Research Funds for the Central Universities (202461001), and Laoshan Laboratory (No. LSKJ202202600). We are thankful to Center for High Performance Computing and System Simulation, Pilot National Laboratory for Marine Science and Technology (Qingdao) for providing computing resource.

Authors' contribution XXT and JPL contributed to the conceptualization and design of the study. Figures visualization and formal analysis were performed by XXT. YNY contributed to the preparation and analysisof the figure Wave Ray Flux. The first draft of the manuscript was written by XXT, and all authors reviewed and approved the manuscript.

Data availability The monthly precipitation data were obtained from the global monthly mean precipitation dataset of the ERA5 (ECMWF; https://cds.climate.copernicus.eu/datasets) (Hersbach et al. 2023). Atmospheric variables were obtained from the National Centers for Environmental Prediction–National Center for Atmospheric Research reanalysis dataset (https://www.psl.noaa.gov/data/gridded/data.ncep.reanalysis.derived.html). The AO index is openly available at the following URL: lijianping.cn/dct/page/1. The Nino 3.4 index was obtained from the NOAA Physical Sciences Laboratory (https://psl.noaa.gov/data/timeseries/month/DS/Nino34/).

Declarations

Conflict of interest The authors declare no conflict of interest.

References

Alexander MA, Bladé I, Newman M, Lanzante JR, Lau NC, Scott JD (2002) The atmospheric bridge: the influence of ENSO teleconnections on air-sea interaction over the global oceans. J Clim 15:2205–2231

Ayarzagüena B, Ineson S, Dunstone NJ, Baldwin MP, Scaife AA (2018) Intraseasonal effects of El Niño-Southern Oscillation on North Atlantic climate. J Clim 31:8861–8873

Bjerknes J (1969) Atmospheric teleconnections from the equatorial Pacific. Mon Wea Rev 97:163–172

Chapman WE, Subramanian AC, Xie SP, Sierks MD, Martin Ralph F, Kamae Y (2021) Monthly modulations of ENSO teleconnections: implications for potential predictability in North America. J Clim 34:5899–5921

Chen W, Lan X, Wang L, Ma Y (2013) The combined effects of the ENSO and the arctic oscillation on the winter climate anomalies in East Asia. Chin Sci Bull 58:1355–1362. https://doi.org/10.1007/s11434-012-5654-5

Cheung HN, Zhou W, Mok HY, Wu MC (2012) Relationship between Ural-Siberian Blocking and the East Asian winter monsoon in

relation to the arctic oscillation and the El Niño-Southern oscillation. J Clim 25:4242–4257. https://doi.org/10.1175/JCLI-D-11-00225.1

Deser C, Simpson IR, McKinnon KA, Phillips AS (2017) The Northern hemisphere extratropical atmospheric circulation response to ENSO: how well do we know it and how do we evaluate models accordingly? J Clim 30:5059–5082

Deser C, Simpson IR, Phillips AS, McKinnon KA (2018) How well do we know ENSO's climate impacts over North America, and how do we evaluate models accordingly? J Clim 31:4991–5014

Gao T, Zhang Q, Luo M (2020) Intensifying effects of El Niño events on winter precipitation extremes in southeastern China. Clim Dyn 54:631–648. https://doi.org/10.1007/s00382-019-05022-6

Gong D, Wang S, Zhu J (2001) East Asian winter monsoon and arctic oscillation. Geophys Res Lett 28:131–144. https://doi.org/10.1029/2000GL012311

Held IM (2001) Stationary and quasi-stationary eddies in the extratropical troposphere: theory. Large-Scale Dyn Process Atmos

Hersbach H, Bell B, Berrisford P, Biavati G, Horányi A, Muñoz Sabater J, Nicolas J, Peubey C, Radu R, Rozum I, Schepers D, Simmons A, Soci C, Dee D, Thépaut J-N (2023) ERA5 monthly averaged data on single levels from 1940 to present. Copernicus Climate Change Service (C3S) Climate Data Store (CDS)

He S, Gao Y, Li F, Wang H, He Y (2017) Impact of arctic oscillation on the East Asian climate: a review. Earth-Sci Rev 164:48–62. https://doi.org/10.1016/j.earscirev.2016.10.014

Horel JD, Wallace JM (1981) Planetary-scale atmospheric phenomena associated with the Southern oscillation. Mon Wea Rev 109:813–829

Hoskins BJ, Ambrizzi T (1993) Rossby wave propagation on a realistic longitudinally varying flow. J Atmos Sci 50:1661–1671

Hoskins BJ, Karoly DJ (1981) The steady linear response of a spherical atmosphere to thermal and orographic forcing. J Atmos Sci 38:1179–1196

Huang B, Thorne PW, Banzon VF, Boyer T, Chepurin G, Lawrimore JH, Menne MJ, Smith TM, Vose RS, Zhang H-M (2017b) Extended reconstructed sea surface temperature, version 5 (ERSSTv5): upgrades, validations, and intercomparisons. J Climate 30:8179–8205

Huang W, Chen R, Yang Z, Wang B, Ma W (2017a) Exploring the combined effects of the arctic oscillation and ENSO on the wintertime climate over East Asia using self-organizing maps. J Geophys Res Atmos 122:9107–9129

Kerr RA (1999) A new force in high latitude climate. Science 284(5412):241–242

King MP, Herceg-Bulić I, Bladé I, GarcíA-Serrano J, KeenlySide N, Kucharski F, Li C, Sobolowski S (2018) Importance of late fall ENSO teleconnection in the Euro-Atlantic sector. Bull Am Meteorol Soc 99:1337–1343

Li C, Sun J (2015) Role of the subtropical westerly jet waveguide in a southern China heavy rainstorm in December 2013. Adv Atmos Sci 32:601–612. https://doi.org/10.1007/s00376-014-4099-y

Li JP (2016) Impacts of annular modes on extreme climate events over the East Asian monsoon region. In: Li J et al (eds) Dynamics and predictability of large-scale, high-impact weather and climate events. Cambridge University Press, United Kingdom, p 370

Li JP, Ren R, Qi Y, Wang F, Lu R, Zhang P, Jiang Z, Duan W, Yu F, Yang Y (2013) Progress in air-land-sea interactions in Asia and their role in global and Asian climate change. Chin J Atmos Sci 37:518–538. https://doi.org/10.3878/j.issn.1006-9895.2012.12322

Li JP, Xie T, Tang X, Wang H, Sun C, Feng J, Zheng F, Ding R (2022) Influence of the NAO on wintertime surface air temperature over the East Asia: multidecadal variability and decadal prediction. Adv Atmos Sci 39(4):625–642. https://doi.org/10.1007/s00376-021-1075-1

Li JP, Zheng F, Sun C, Feng J, Wang J (2019b) Pathways of influence of the Northern Hemisphere mid-high latitudes on East Asian climate: a review. Adv Atmos Sci 36:902–921. https://doi.org/10.1007/s00376-019-8236-5

Li J, Wang JXL (2003) A new North Atlantic Oscillation index and its variability. Adv Atmos Sci 20:661–676. https://doi.org/10.1007/BF02915394

Li YJ, Feng J, Li JP, Hu AX (2019a) Equatorial windows and barriers for stationary Rossby wave propagation. J Clim 32:6117–6135. https://doi.org/10.1175/JCLI-D-18-0722.1

Li YJ, Li JP (2012) Propagation of planetary waves in the horizontal non-uniform basic flow. Chin J Geophys 55:361–371. https://doi.org/10.6038/j.issn.0001-5733.2012.02.001. (**in Chinese**)

Li YJ, Li JP, Jin F-F, Zhao S (2015) Interhemispheric propagation of stationary Rossby waves in a horizontally nonuniform background flow. J Atmos Sci 72:3233–3256. https://doi.org/10.1175/JAS-D-14-0239.1

Li Y, Lau NC (2012) Impact of ENSO on the atmospheric variability over the North Atlantic in late winter-role of transient eddies. J Clim 25(1):320–342

Luo D et al (2016) Impact of Ural blocking on winter warm Arctic-cold Eurasian anomalies. Part II: the link to the North Atlantic oscillation. J Clim 29:3949–3971. https://doi.org/10.1175/JCLI-D-15-0612.1

Mao R, Gong D, Yang J, Bao J (2011) Linkage between the arctic oscillation and winter extreme precipitation over central-southern China. Clim Res 50:187–201. https://doi.org/10.3354/cr01041

Park TW, Ho CH, Yang S (2011) Relationship between the arctic oscillation and cold surges over East Asia. J Clim 24:68–83. https://doi.org/10.1175/2010JCLI3529.1

Qi X, Li JP, Zhao Y, Hou ZL, Zhang YZ (2025) Synergistic role of Atlantic SST and southern Russian steppe precipitation in subseasonal heat prediction over the Yangtze River Basin. Clim Dyn 63:120

Sardeshmukh, P. D., and B. J. Hoskins, 1988: The Generation of Global Rotational Flow by Steady Idealized Tropical Divergence. J. Atmos. Sci., 45, 1228–1251

Scaife AA, Comer RE, Dunstone NJ, Knight JR, Smith DM, MacLachlan C, Martin N, Peterson KA, Rowlands D, Carroll EB, Belcher S, Slingo J (2017) Tropical rainfall, Rossby waves and regional winter climate predictions. Q J R Meteorol Soc 143(702):1–11. https://doi.org/10.1002/qj.2910

Song J, Yang H, Li C (2011) A further study of causes of the severe drought in Yunnan Province during the 2009/2010 winter. Chin J Atmos Sci 35(6):1009–1019. https://doi.org/10.3878/j.issn.1006-9895.2011.06.02

Sun Y, Li J (2022) Synergistic effect of El Niño and the North Pacific oscillation on wintertime precipitation over Southeastern China and the East China Sea Kuroshio area. Clim Dyn 58:1635–1649. https://doi.org/10.1007/s00382-021-05982-8

Takaya K, Nakamura H (2001) A formulation of a phase-independent wave-activity flux for stationary and migratory quasigeostrophic eddies on a zonally varying basic flow. J Atmos Sci 58:608–627

Tang XX, Li JP (2024) Synergistic effect of boreal autumn SST over the tropical and South Pacific and winter NAO on winter precipitation in the southern Europe. NPJ Clim Atmos Sci 7:1–14. https://doi.org/10.1038/s41612-024-00628-y

Tang XX, Li JP, Zhang YZ, Li YJ, Zhao S (2023) Synergistic effect of El Nino and negative phase of NAO on winter precipitation in the southeastern United States. J Clim 36:1767–1791. https://doi.org/10.1175/JCLI-D-22-0293.1

Thompson DWJ, Wallace JM (1998) The arctic oscillation signature in the wintertime geopotential height and temperature fields. Geophys Res Lett 25:1297–1300

Thompson DWJ, Wallace JM (2001) Regional climate impacts of the Northern Hemisphere annular mode. Science 293:85–89

Trenberth KE, Branstator GW, Karoly D, Kumar A, Lau N-C, Ropelewski C (1998) Progress during TOGA in understanding and modeling global teleconnections associated with tropical sea surface temperatures. J Geophys Res 103:14291–14324

Wallace JM, Gutzler DS (1981) Teleconnections in the geopotential height field during the Northern Hemisphere winter. Mon Wea Rev 109:784–812

Wang HJ, Zhang RH, Cole J, Chavez F (1999) El Nino and the related phenomenon Southern Oscillation (ENSO): the largest signal in interannual climate variation. Proc Natl Acad Sci USA 96:11071–11072

Wang H, Li J, Zheng F, Li F (2023) The synergistic effect of the summer NAO and northwest Pacific SST on extreme heat events in the central–eastern China. Clim Dyn 61:4283–4300

Wang H, Li J, Zheng F, Li F, Wang N, Sun Y (2024) The synergistic effect of the preceding winter mid-latitude North Atlantic and summer tropical eastern Indian Ocean SST on summer extreme heat events in northern China. Weather Clim Extremes 44:2212-0974

Wang H, Zheng F, Diao Y, Li J, Sun R, Tang X, Sun Y, Li F, Zhang Y (2022) The synergistic effect of the preceding winter Northern Hemisphere annular mode and spring tropical North Atlantic SST on spring extreme cold events in the mid-high latitudes of East Asia. Clim Dyn 59:3175–3191

Watanabe M (2004) Asian jet waveguide and a downstream extension of the North Atlantic oscillation. J Clim 17:4674–4691. https://doi.org/10.1175/JCLI-3228.1

Wei J, Zhang J (2021) Influence of the position and kinetic energy anomalies of the inlet region of the Asian-African subtropical westerly jet on the mid-summer interdecadal drought in North China. Plateau Meteorol 40(2):281–291. https://doi.org/10.7522/j.issn.1000-0534.2020.00043

Wen M, Yang S, Kumar A, Zhang P (2009) An analysis of the large-scale climate anomalies associated with the snowstorms affecting China in January 2008. Mon Weather Rev 137:1111–1131. https://doi.org/10.1175/2008MWR2638.1

Wu Z, Lin H (2012) Interdecadal variability of the ENSO-North Atlantic oscillation connection in boreal summer. Q J R Meteorol Soc 138:1668–1675. https://doi.org/10.1002/qj.1889

Wu Z, Zhang P (2015) Interdecadal variability of the mega-ENSO-NAO synchronization in winter. Clim Dyn 45:1117–1128. https://doi.org/10.1002/qj.1889

Xie TJ, Li JP, Sun C, Ding RQ, Wang KC, Zhao CF, Feng J (2019) NAO implicated as a predictor of the surface air temperature multidecadal variability over East Asia. Clim Dyn 53:895–905

Xu, HL (2013) Impacts of Southern Eurasian teleconnection pattern and Atlantic-Eurasian teleconnection pattern on the rainfall over China in winter and autumn. Ph.D. dissertation, Chinese Academy of Science, p 124

Xu H, Li J, Feng J, Mao J (2012) The asymmetric relationship between the winter NAO and the precipitation in Southwest China. Acta Meteorol Sin 70(6):1276–1291. https://doi.org/10.11676/qxxb2012.107

Xu K, Zhu CW, He JH (2013) Two types of El Niño-related Southern oscillation and their different impacts on global land precipitation. Adv Atmos Sci 30(6):1743–1757

Yang Y, Li J (2025) Novel monsoon indices based on vector projection and directed angle for measuring the East Asian summer monsoon. Clim Dyn 63:210. https://doi.org/10.1007/s00382-025-07696-7

Zhang RH, Sumi A (2002) Moisture circulation over East Asia during El Nino episode in Northern winter, spring and autumn. J Meteorol Soc Jpn 80:213–227

Zhang RH, Sumi A, Kimoto M (1999) A diagnostic study of the impact of El Niño on the precipitation in China. Adv Atmos Sci 16:229–241

Zhang R, Min Q, Su J (2017) Impact of El Niño on atmospheric circulations over East Asia and rainfall in China: role of the anomalous western North Pacific anticyclone. Sci China Earth Sci 60:1124–1132. https://doi.org/10.1007/s11430-016-9026-x

Zhang W, Wang Z, Stuecker MF et al (2019) Impact of ENSO longitudinal position on teleconnections to the NAO. Clim Dyn 52:257–274. https://doi.org/10.1007/s00382-018-4135-1

Zhao S, Li J, Li Y (2015) Dynamics of an interhemispheric teleconnection across the critical latitude through a southerly duct during boreal winter. J Clim 28:7437–7456. https://doi.org/10.1175/JCLI-D-14-00425.1

Zhao S, Li J, Li Y, Jin FF, Zheng J (2019) Interhemispheric influence of Indo-Pacific convection oscillation on Southern Hemisphere rainfall through southward propagation of Rossby waves. Clim Dyn. https://doi.org/10.1007/s00382-018-4324-y

Zhou L, Tam C, Zhou W, Chan J (2010) Influence of South China Sea SST and the ENSO on winter rainfall over South China. Adv Atmos Sci 27:832–844. https://doi.org/10.1007/s00376-009-9102-7

Zuo J (2011) Relationship between AO/NAO and ENSO and their impact on climate anomalies in China. Dissertation, Lanzhou University pp 55–62